

The flattening and the orbital structure of early-type galaxies and collisionless N -body binary disk mergers

J. Thomas^{1,2*}, R. Jesseit¹, R. P. Saglia^{1,2}, R. Bender^{1,2}, A. Burkert¹,
E. M. Corsini³, K. Gebhardt⁴, J. Magorrian⁵, T. Naab¹,
D. Thomas⁶ and G. Wegner⁷

¹Universitätssternwarte München, Scheinerstraße 1, D-81679 München, Germany

²Max-Planck-Institut für Extraterrestrische Physik, Giessenbachstraße, D-85748 Garching, Germany

³Dipartimento di Astronomia, Università di Padova, vicolo dell'Osservatorio 3, I-35122 Padova, Italy

⁴Department of Astronomy, University of Texas at Austin, C1400, Austin, TX78712, USA

⁵Theoretical Physics, Department of Physics, University of Oxford, 1 Keble Road, Oxford U.K., OX1 3NP

⁶Institute of Cosmology and Gravitation, Mercantile House, University of Portsmouth, Portsmouth, PO1 2EG, UK

⁷Department of Physics and Astronomy, 6127 Wilder Laboratory, Dartmouth College, Hanover, NH 03755-3528, USA

Submitted to MNRAS —; Accepted —

ABSTRACT

We use oblate axisymmetric dynamical models including dark halos to determine the orbital structure of intermediate mass to massive Coma early-type galaxies. We find a large variety of orbital compositions. Averaged over all sample galaxies the unordered stellar kinetic energy in the azimuthal and the radial direction are of the same order, but they can differ by up to 40 percent in individual systems. In contrast, both for rotating and non-rotating galaxies the vertical kinetic energy is on average smaller than in the other two directions. This implies that even most of the rotating ellipticals are flattened by an anisotropy in the stellar velocity dispersions. Using three-integral axisymmetric toy models we show that flattening by stellar anisotropy maximises the entropy for a given density distribution. Collisionless disk merger remnants are radially anisotropic. The apparent lack of strong radial anisotropy in observed early-type galaxies implies that they may not have formed from mergers of disks unless the influence of dissipational processes was significant.

Key words: galaxies: kinematics and dynamics – galaxies: elliptical and lenticular, cD – galaxies: formation

1 INTRODUCTION

The way in which a galaxy has assembled its stars is reflected in the distribution of stellar orbits. For example, collisionless N -body collapse simulations predict a predominance of radial orbits in the final remnant (van Albada 1982). In contrast, collisionless galaxy merger simulations predict a variety of orbital compositions, depending on progenitor properties (Barnes 1992; Hernquist 1992, 1993), the merging geometry (Weil & Hernquist 1996; Dubinski 1998), the progenitor mass ratios (Naab & Burkert 2003; Jesseit, Naab & Burkert 2005) and the presence of dissipational components (Naab, Jesseit & Burkert 2006; Jesseit et al. 2007). Stars in galaxies are approximately collisionless and the orbital structure – once a galaxy has approached a quasi-steady-state – is conserved for a long time.

To a certain extent then, the assembly mechanism of early-type galaxies can be constrained from their present-day orbital structure.

A global characteristic of the distribution of stellar orbits is its anisotropy. Traditionally, anisotropies of elliptical galaxies have been inferred from the $(v/\sigma, \epsilon)$ diagram. In particular, the rotation of bright ellipticals has been shown to be insufficient to account for their flattening (Binney 1978). However, whether fainter, fast-rotating ellipticals are flattened by rotation is less easy to determine from the $(v/\sigma, \epsilon)$ diagram, because isotropic as well as anisotropic systems can rotate. In fact, fully general axisymmetric dynamical models recently have revealed an anisotropic orbital structure in even the flattest, fast rotating objects (Cappellari et al. 2007). One goal of this paper is to investigate numerically the connection between anisotropy, rotation and flattening in spheroidal stellar systems.

* E-mail: jthomas@mpe.mpg.de

In addition, we present global anisotropies for a sam-

ple of Coma early-type galaxies. These anisotropies are derived by analysing long-slit stellar absorption line kinematics with axisymmetric orbit models. Our dynamical models include dark matter halos. Previous anisotropy determinations for larger samples of ellipticals (including dark matter) were restricted to round and non-rotating systems, assuming spherical symmetry (Gerhard et al. 2001; Magorrian & Ballantyne 2001). Spherical models do not account for galaxy flattening. In the simplest case, a flattened system is axially symmetric. Early axisymmetric models, however, did not cover all possible anisotropies (and orbital structures, respectively; e.g. Carollo et al. 1995). Fully general, orbit-based axisymmetric dynamical models have so far only been applied to the inner regions of ellipticals and the orbital analysis was made under the assumption that mass follows light (e.g. Gebhardt et al. 2003 and Cappellari et al. 2006). By the mass-anisotropy degeneracy, the neglect of dark matter could translate to a systematic bias in the corresponding orbital structure (e.g. Forestell & Gebhardt 2008). Comparison of anisotropies derived with and without dark matter will allow one to quantify such a possible bias.

We also discuss anisotropies derived from modelling mock observations of synthetic N -body merger remnants. One motivation to do so is that dynamical models of axisymmetric systems may not be unique. For example, the deprojection of an axisymmetric galaxy is intrinsically degenerate (Rybicki 1987). Uncertainties in the intrinsic shape thereby propagate into uncertainties on the derived masses and anisotropies (e.g. Thomas et al. 2007a). Moreover, the reconstruction of an axisymmetric orbital system is suspected to be further degenerate with the recovered mass (e.g. the discussion in Valluri, Merritt & Emsellem 2004). The case for a generic degeneracy, beyond the effects of noise and incompleteness of the data, is still uncertain (e.g. Magorrian 2006). Numerical studies of a few idealised axisymmetric toy models indicate degeneracies to be moderate when modelling realistically noisy data sets (Krajnović et al. 2005, Thomas et al. 2005). Since we know the true structure of our N -body modelling targets, we can extend on these studies and further investigate potential systematics in the models over a broader sample of test cases.

Another motivation to model N -body merger remnants is to probe whether ellipticals have formed by merging. This requires a comparison of the orbital structure in real ellipticals with predictions of N -body simulations (e.g. Burkert & Naab 2005; Burkert et al. 2008). However, because of the symmetry assumptions in models of real galaxies, it is not straight forward to compare *intrinsic* properties of N -body simulations with *models* of real galaxies. To avoid the related systematics, we here compare models of real galaxies with *similar models* of synthetic N -body merger simulations and both are indicative for true differences between real galaxies and merger predictions.

The galaxy and N -body merger samples and the modelling technique are briefly outlined in Sec. 2. Toy models of various flattening and anisotropy are discussed in Sec. 3. The anisotropies of real galaxies are presented in Sec. 4 and compared with models of N -body merger remnants in Sec. 5. Implications for the formation process of early-type galaxies are discussed in Sec. 6 and we summarise our results in Sec. 7. The influence of regularisation and the inclusion of dark matter halos on reconstructed galaxy anisotropies

GMP (1)	NGC (2)	ϵ (3)	δ (4)	β (5)	γ (6)	$(v/\sigma)^*$ (7)
0144	4957	0.48	0.44	0.36	-0.27	0.42
0282	4952	0.57	0.39	0.45	0.17	0.64
0756	4944	0.61	0.22	0.29	0.10	0.83
1176	4931	0.65	0.22	0.22	-0.16	0.91
1750	4926	0.17	0.21	0.26	0.11	0.17
1990	IC 843	0.54	-0.03	0.13	0.16	1.11
2417	4908	0.28	0.14	0.24	0.21	1.02
2440	IC 4045	0.58	-0.08	0.06	0.07	1.51
2921	4889	0.35	0.19	0.31	0.30	0.09
3329	4874	0.11	0.05	-0.12	-0.36	0.63
3414	4871	0.42	0.16	0.18	0.04	0.97
3510	4869	0.17	0.13	0.13	-0.01	0.71
3792	4860	0.28	0.17	0.13	-0.08	0.29
3958	IC 3947	0.36	0.20	0.12	-0.21	1.03
4822	4841A	0.22	0.12	0.20	0.17	0.41
4928	4839	0.34	0.30	0.31	0.02	0.39
5279	4827	0.23	0.15	0.16	0.02	0.39
5568	4816	0.22	0.21	0.36	0.37	0.27
5975	4807	0.21	0.06	0.05	-0.03	1.29

Table 1. Summary of COMA galaxy anisotropies. (1-2): galaxy id (GMP numbers from Godwin, Metcalfe & Peach 1983); (3): intrinsic ellipticity ϵ ; (4-6): anisotropy parameters δ , β and γ (cf. equations 5-7) of the best-fit dynamical model; (7): $(v/\sigma)^*$, i.e. (v_{\max}/σ_o) normalised by the approximate value $\sqrt{\epsilon_{\text{obs}}/(1 - \epsilon_{\text{obs}})}$ of an (edge-on) isotropic rotator with the same flattening. Note that $(v/\sigma)^*$ is an observable, i.e. it combines *observed* ellipticities ϵ_{obs} (from column 10 of Tab. 1 of Mehlert et al. 2000) and observed velocities v_{\max} and σ_o , without reference to any dynamical model.

is discussed in App. A. In App. B we briefly discuss the connection between anisotropy and the shape of the circular velocity curve in maximum entropy models. We assume that the Coma cluster is at a distance of 100 Mpc.

2 DATA AND BASIC DEFINITIONS

A complete description of a stellar system is given by its distribution function f (DF; the density in 6-dimensional phase-space). In a steady-state system the DF f depends on the phase-space coordinates only through the integrals of motion (Lynden-Bell 1962). Axisymmetric potentials, which are considered here, admit the two classical integrals of motion energy (E) and z-component of the angular momentum (L_z). In addition, many orbits in astrophysically relevant potentials are characterised by another, non-classical, so-called third integral (I_3 ; Contopoulos 1963). Since integrals of motion label orbits and vice-versa, a steady-state system can be viewed as a superposition of orbits, each with constant phase-space density. Let $f(i)$ denote the phase-space density along orbit i , then the total amount of light $w(i)$ on the orbit equals $w(i) = f(i) \times V(i)$ ($V(i)$ is the orbit's phase-space volume). The DF – or the weights of a suitable orbit superposition model – determine the spatial density ρ and intrinsic velocity dispersions σ via

$$\rho = \int f d^3v \quad (1)$$

and

$$\sigma_{ij}^2 = \frac{1}{\rho} \int f (v_i - \bar{v}_i)(v_j - \bar{v}_j) d^3v, \quad (2)$$

$$\bar{v}_i = \frac{1}{\rho} \int f v_i d^3v. \quad (3)$$

In the following we will only consider $i, j \in \{z, x, \phi, R\}$, where z is the short axis of the density distribution, ϕ is the azimuth around this axis, x is a fixed Cartesian coordinate parallel to the equatorial plane and R is a cylindrical radius. Let

$$\Pi_{ii} = \int \rho \sigma_{ii}^2 d^3r \quad (4)$$

denote the total¹ (unordered) kinetic energy in coordinate direction i , then the global anisotropy of an axisymmetric stellar system can be quantified, for example, by the ratios

$$\delta \equiv 1 - \frac{\Pi_{zz}}{\Pi_{xx}} \quad (5)$$

$$\beta \equiv 1 - \frac{\Pi_{zz}}{\Pi_{RR}} \quad (6)$$

and

$$\gamma \equiv 1 - \frac{\Pi_{\phi\phi}}{\Pi_{RR}} \quad (7)$$

(Cappellari et al. 2007). In axisymmetric systems, the three anisotropy parameters are related via

$$\delta = \frac{2\beta - \gamma}{2 - \gamma}. \quad (8)$$

Non-rotating, isotropic spherical systems as well as classical isotropic rotators obey $\delta = \beta = \gamma = 0$.

The DF of real galaxies is not known, but has to be reconstructed from photometric and kinematic observations. In the next two subsections we will describe the two samples of real and simulated galaxies discussed in this paper and will briefly outline our modelling method.

2.1 Coma early-types

Our sample of observed galaxies (COMA in the following) consists of 19 Coma early-types from Thomas et al. (2007b, 2008). It comprises 2 central cD galaxies, 10 ordinary giant ellipticals and 7 S0 or intermediate galaxies with luminosities $-20.3 \geq M_B \geq -22.56$ (a single fainter object with $M_B = -18.8$ is also included in the sample). The galaxies are drawn from the luminosity limited sample of Mehlert et al. (2000) and are distributed all over the cluster. High-resolution radial profiles of surface brightness, ellipticity and isophotal shape parameters a_4 and a_6 (up to a_{12} in some cases; cf. Bender & Möllenhoff 1987 for a definition of the isophotal shape parameters) derived from a combination of HST and ground-based imaging were used to calculate the deprojected 3d luminosity distribution for several inclinations. The photometric data are complemented by long-slit stellar absorption line kinematics along 2 – 4 position-angles per galaxy. The kinematic data consists of radial

profiles of mean velocity, velocity dispersion and higher-order moments of the line-of-sight velocity distribution and reach out to $1 - 4r_{\text{eff}}$. Details about the photometric and kinematic data can be found in Jørgensen & Franx (1994), Mehlert et al. (2000), Wegner et al. (2002), Corsini et al. (2008) and Thomas et al. (2008).

These data were modelled with our implementation of Schwarzschild's (1979) orbit superposition technique for axisymmetric potentials (Richstone & Tremaine 1988; Gebhardt et al. 2000, 2003; Thomas et al. 2004). For each galaxy, we probed for a variety of mass models, composed of a stellar mass density (from the deprojected light profile) and a parametric dark halo profile. The parameter space for the mass models spans the inclination, the stellar mass-to-light ratio and the dark halo parameters. In each trial potential the best-fit orbit model is calculated by maximising

$$S - \alpha\chi^2, \quad (9)$$

where χ^2 quantifies deviations between observed and modelled kinematics². The function

$$S = - \sum w(i) \ln \frac{w(i)}{\Omega(i)} \quad (10)$$

is used to smooth the orbit models. In the absence of any other constraints the maximisation of S yields orbital weights $w(i) \propto \Omega(i)$ (Richstone & Tremaine 1988), such that the yet not specified $\Omega(i)$ can be regarded as weight-factors for the $w(i)$. When modelling real galaxies or mock observations of N -body merger remnants, we assume that there is no preferred region in phase-space and each orbit is given an a priori-weight equal to its phase-space volume: $\Omega(i) \equiv V(i)$. Then,

$$S = - \sum w(i) \ln \frac{w(i)}{V(i)} \approx - \int f \ln f d^3r d^3v \quad (11)$$

equals the Boltzmann entropy, which drives models towards a constant density in phase-space.

The (binned) deprojected luminosity density is used as a boundary condition to solve equation (9) and the regularisation parameter α in equation (9) has been calibrated by means of Monte-Carlo simulations (Thomas et al. 2005). The final, best-fit orbit model is obtained from a χ^2 -analysis.

2.2 N -body merger remnants

We have applied the same modelling code to mock observations of synthetic N -body merger simulations. In brief, we have modelled six merger remnants, each projected along its three principal axes (models of projections along the long, intermediate and short axis of the merger remnants will be shortly referred to as X, Y and Z-models later on). The six merger remnants are taken from the sample of collisionless disk+bulge+halo mergers of Naab & Burkert (2003). They have mass ratios between 1:1 and 4:1 and sample the entire distribution of intrinsic shapes and orbital make-ups, including extreme cases. An orbital analysis of the N -body

¹ In the following we will only consider anisotropies (and kinetic energies, respectively) inside the effective radius, because this is the radius inside which kinematical observations are typically available to constrain the orbital structure of real galaxies.

² We use the full information of (binned) line-of-sight velocity distributions when fitting real galaxies and N -body merger remnants.

systems is given in Jesseit, Naab & Burkert (2005). We have simulated typical Coma observations for each projection: the merger remnants were placed at a distance of 100 Mpc and photometric and kinematic profiles with similar resolution and spatial coverage as in the COMA sample have been extracted. For a detailed discussion of the models the reader is referred to Thomas et al. (2007a).

3 TOY MODELS

Oblate stellar systems can owe their shapes to a variety of different orbital configurations. Classically, one has often distinguished between two proto-typical cases: flattening by rotation and flattening by anisotropy. Thereby, flattening by rotation is used to term an otherwise round and isotropic system which appears flattened – and rotating – by extra-light on near-equatorial, high angular-momentum orbits (populated with the same sense of rotation). Flattening by anisotropy refers to systems with a depression of stars with high velocities perpendicular to the equatorial plane ($\Pi_{zz} < \Pi_{RR} = \Pi_{\phi\phi}$). However, in fact there are infinitely many orbit superpositions that account for a given galaxy shape. Some of these are discussed in Dehnen & Gerhard (1993). Different orbital structures can be distinguished by their different anisotropies. In the following we will numerically construct (self-consistent) toy models that are designed to (1) reproduce a given, flattened, density distribution exactly, but (2) have different intrinsic anisotropies.

3.1 Self-consistent models without rotation

The models are orbit-based and similar to those described in Sec. 2. However, here we only require the models to reproduce a given density ($\alpha = 0$ in equation 9). Various expressions for the factors $\Omega(i)$ in equation (10) will be used to impose different anisotropy structures (see below).

For our simple toy models we assume a stellar density

$$\rho \propto m^{-1}(m+1)^{-3} \quad (12)$$

(Hernquist 1990) with

$$m^2 = R^2 + \frac{z^2}{q^2}. \quad (13)$$

Equations (12) and (13) describe systems with constant flattening q . They approximate the light profiles of elliptical galaxies reasonably well.

Flattening and maximum entropy. Let f_S denote the DF that maximises the entropy of equation (11) subject to the density constraints. The squares in the top panel of Fig. 1 illustrate the connection between anisotropy and flattening for f_S : the three panels show the anisotropy parameters from equations (5-7) as a function of the intrinsic ellipticity $\epsilon \equiv 1 - q$ (cf. equation 13). While δ and β increase with flattening, γ is roughly constant. In maximum-entropy models the flattening thus arises from a suppression of energy in z -direction, while the balance between the energies in R and ϕ is roughly conserved. In this sense, the maximum entropy models f_S resemble the classical case of flattening by anisotropy. The only difference is that $\gamma \neq 0$ (cf. App. B

for a discussion of γ). Note that we calculated the toy models with the same library setup as used for the Coma galaxy models.

Flattening by a classical $f = f(E, L_z)$. A classical two-integral DF f_{2I} , which only depends on E and L_z , can be approximated via equations (9,10) with

$$\Omega(i) = \frac{C(i)}{1 - C(i)} \sum_{j \in \mathcal{J}(i), j \neq i} w(j), \quad (14)$$

$$C(i) = V(i) \left(\sum_{j \in \mathcal{J}(i)} V(j) \right)^{-1} \quad (15)$$

and

$$\mathcal{J}(i) = \{j \in \{1, \dots, N\} : L_z(j) = L_z(i), E(j) = E(i)\} \quad (16)$$

(N is the total number of orbits). Equation (14) derives from the constraint that for $f_{2I} \approx f(E, L_z)$, the phase-space density of any orbit i with energy $E(i)$ and angular momentum $L_z(i)$ has to equal the mean phase-space density of all orbits j with the same $E(i) = E(j)$ and $L_z(i) = L_z(j)$, i.e.

$$f(i) = \frac{w(i)}{V(i)} \approx \frac{\sum_{j \in \mathcal{J}(i)} w(j)}{\sum_{j \in \mathcal{J}(i)} V(j)}. \quad (17)$$

This case is included in Fig. 1 by the circles. That the $\Omega(i)$ from equation (14) indeed yield $f \approx f(E, L_z)$ is demonstrated by $\beta \approx 0$. The flattening of the corresponding systems comes from an excess energy in ϕ -direction with respect to the isotropic case ($\gamma < 0$; orbits with high angular momentum are strongly populated). The relationship between δ and ϵ is similar as in maximum entropy models.

Note that DFs $f \approx f(E, L_z)$ develop noticeable phase-space density peaks on orbits with high angular momentum (Dehnen & Gerhard 1994). It is likely this property that lowers their entropy as compared to the f_S models. Flattening by anisotropy mainly involves shell orbits which approach closely the intrinsic minor-axis. Their phase-space volumes are much larger than those of equatorial near-circular orbits with high angular momentum. Even a small change in the phase-space density along shell orbits can reduce the amount of light near the minor-axis considerably and, thus, result in a significant flattening. The larger fraction of phase-space involved in this type of flattening, compared with a strong overpopulation of the relatively small region in phase-space occupied by near-circular orbits (as in cases where $f = f(E, L_z)$) explains why objects which are flattened by anisotropy have the higher entropy.

Flattening with radial anisotropy. Model DFs f_{rad} obtained with

$$\Omega(i) = [r_{\text{apo}}(i) - r_{\text{peri}}(i)]^4 \times V(i) \quad (18)$$

are biased towards orbits with a large difference $r_{\text{apo}} - r_{\text{peri}}$ between apocentre and pericentre radius (radially extended orbits). Such models are radially anisotropic ($\beta, \gamma > 0$; cf. triangles in Fig. 1). The relationship between δ and ϵ is again similar as in the previous models.

The latter is no surprise, as for self-consistent ellipsoids with constant flattening, $\delta(\epsilon)$ can be calculated from the tensor virial theorem (Roberts 1962; Binney & Tremaine 1987):

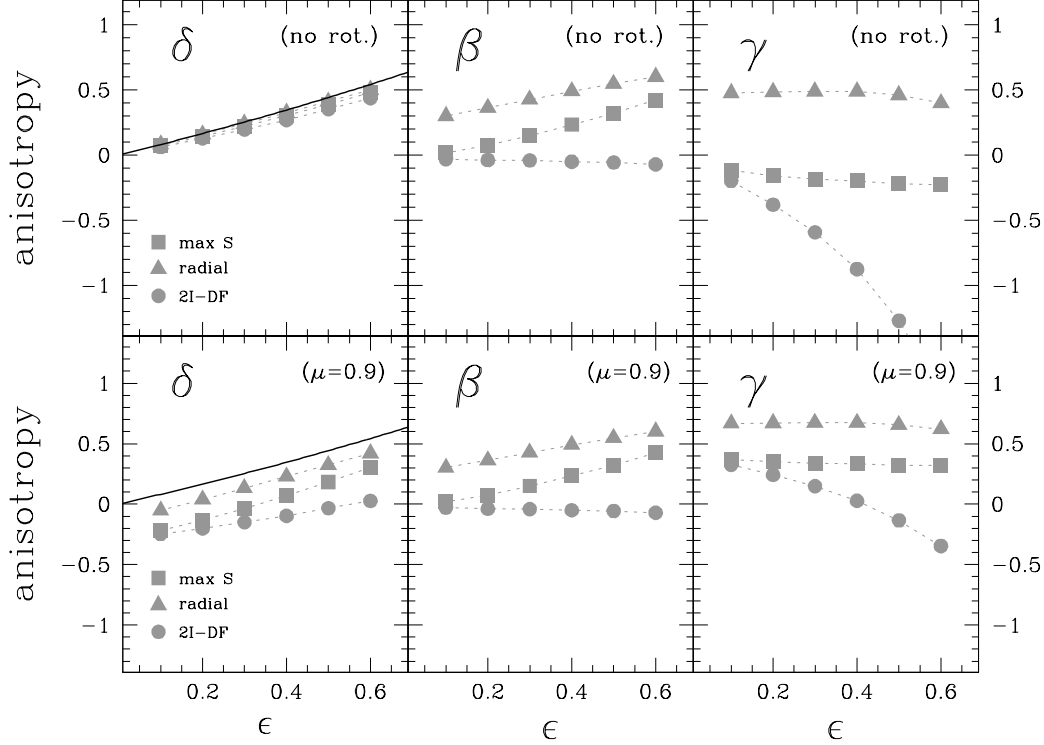


Figure 1. Anisotropy parameters δ , β and γ (as labelled in the panels) versus intrinsic ellipticity ϵ for the toy models f_S (squares), f_{2I} (circles) and f_{rad} (triangles). Toy models of the same type are connected by dotted lines. Top: models without rotation; bottom: models with rotation ($\mu = 0.9$; cf. equation 24); light symbols: without dark matter halo; solid lines: tensor virial theorem applied to oblate spheroids with constant flattening.

$$\delta(\epsilon) = 1 - \frac{1}{q(e)}, \quad (19)$$

where

$$q(e) = \frac{0.5}{1 - e^2} \times \frac{\arcsin(e) - e\sqrt{1 - e^2}}{e(1 - e^2)^{-0.5} - \arcsin(e)} \quad (20)$$

and

$$e = \sqrt{1 - (1 - \epsilon)^2}. \quad (21)$$

The solid line in the upper-left panel of Fig. 1 shows relation (19). Our numerically constructed orbit models follow this line well.

Note that, if N DFs f_i project each to the same spatial density, then any convex linear combination $f_\lambda = \sum \lambda_i f_i$ with $\sum \lambda_i = 1$ will do so. The properties of f_λ will be intermediate between those of the individual f_i .

3.2 Rotation

The just discussed toy models (and any linear combination of them) are non-rotating, because in our choices for $\Omega(i)$ we haven't distinguished between prograde and retrograde orbits. A large variety of rotation patterns can be constructed from any DF f as follows: each orbit in an axisymmetric potential comes in two flavours, one prograde (with positive $L_z > 0$) and one retrograde ($L_z < 0$). Both share the

same spatial shape but differ only in the sign of the velocity component around the axis of symmetry. Thus, the spatial density will only depend on the sum

$$f^+(E, L_z, I_3) \equiv f(E, L_z, I_3) + f(E, -L_z, I_3), \quad (22)$$

of light on corresponding prograde and retrograde orbits. The amount of rotation, instead, will depend on the difference between the population of the prograde and retrograde orbits, respectively. This can be quantified, for example, by the fraction μ of light on the prograde of each orbit pair:

$$\mu(E, L_z, I_3) = \frac{f(E, L_z, I_3)}{f^+(E, L_z, I_3)} \quad (23)$$

($L_z \geq 0$). For simplicity, let's assume from now on that μ is the same for all orbits. Then, any

$$f_\mu(E, L_z, I_3) \equiv \begin{cases} \mu f^+(E, L_z, I_3) & : L_z \geq 0 \\ (1 - \mu) f^+(E, -L_z, I_3) & : L_z < 0 \end{cases} \quad (24)$$

with $\mu \in [0, 1]$ (to remain positive definite) will give rise to the same density profile as f ($f_\mu^+ \equiv f^+$), but with different degrees of internal rotation. For example, in case of $\mu \equiv 1/2$ prograde and retrograde orbits are populated equally and there will be no rotation in the corresponding system. With $\mu \equiv 1$ ($\mu \equiv 0$) only prograde (retrograde) orbits are populated (maximum rotation).

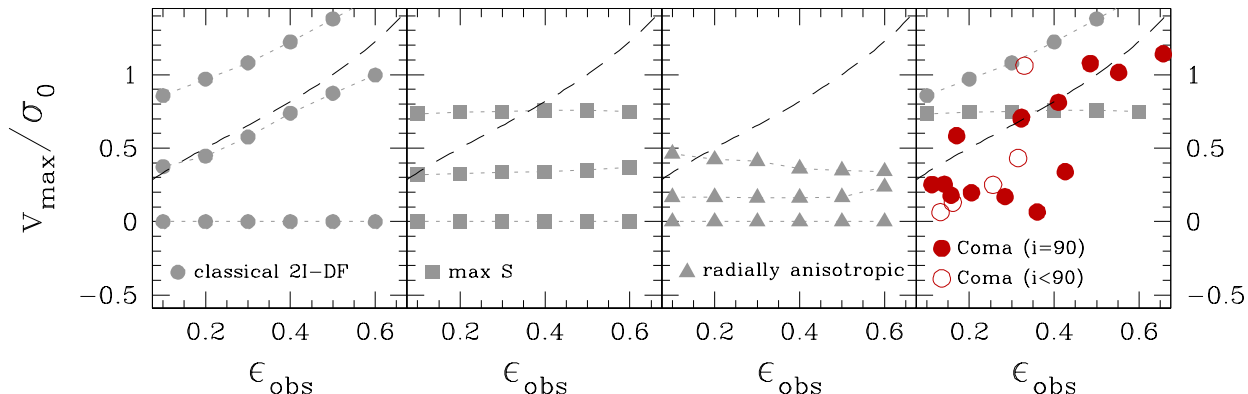


Figure 2. First three panels, from left to right: ellipticity ϵ_{obs} versus classical v/σ for the toy models f_{2I} (grey circles), f_S (grey squares) and f_{rad} (grey triangles). For each toy model the cases $\mu = 0.5, 0.7, 1.0$ (no rotation, intermediate and maximum rotation) are shown. Models with the same μ are connected by the dotted lines. All toy models are edge-on such that $\epsilon_{\text{obs}} = \epsilon$. Outer right panel: ϵ_{obs} versus v/σ for Coma galaxies (filled circles: edge-on galaxies, open circles: non edge-on galaxies). For comparison, the maximally rotating f_{2I} and f_S models are also shown in the outer right panel. In all panels, the dashed lines approximate edge-on isotropic rotators (cf. equation 25).

The bottom panel of Fig. 1 shows anisotropies for the toy models of Sec. 3.1 with $\mu = 0.9$. While β is independent of the amount of rotation, δ decreases and γ increases with increasing rotation. The latter reflects that in our toy models the total energy in ϕ -direction is constant. Any increase of the ordered motion is thus to the expense of a smaller σ_ϕ .

Fig. 2 illustrates where the toy models appear in the $(v/\sigma, \epsilon)$ diagram. The figure shows the three cases $\mu = 0.5$ (no rotation), $\mu = 0.7$ (intermediate rotation) and $\mu = 1.0$ (maximum rotation). On the y-axis, the ratio v_{max}/σ_0 of the maximum rotation velocity (v_{max} , along the projected major-axis) and the central velocity dispersion (σ_0 , averaged inside $r_{\text{eff}}/2$) is shown. All models are edge-on. The highest rotation rates at a given flattening are obtained for f_{2I} , because of its strongly populated high angular momentum orbits ($\Pi_{\phi\phi} > \Pi_{RR} \approx \Pi_{zz}$). However, f_S models, which are not flattened by an excess of light on high angular momentum orbits (relative to the isotropic case) but instead by a suppression of orbits with large z -velocities ($\Pi_{zz} < \Pi_{RR} \approx \Pi_{\phi\phi}$) can reach $(v_{\text{max}}/\sigma_0) \approx 0.75$ as well. The dashed lines in Fig. 2 approximate classical isotropic rotators by

$$\left(\frac{v_{\text{max}}}{\sigma_0}\right)_{\text{iso}} \equiv \sqrt{\frac{\epsilon}{1-\epsilon}} \quad (25)$$

(Kormendy 1982). Up to $\epsilon \approx 0.4$, f_S models can appear in the same region as classical isotropic rotators, although they are not flattened by rotation in the classical sense (e.g. $\beta \neq 0$). Radially anisotropic models are dominated by orbits with low angular momentum and have generally low rotation rates.

A complete picture of an axisymmetric galaxy’s flattening mechanism requires knowledge of the amount of rotation (e.g. v/σ) and at least one anisotropy parameter (e.g. β , γ or δ or the parameter α in the notation of Binney 2005). Alternatively, two anisotropy parameters also specify the global orbital structure. In any case, the full information about the anisotropy and the flattening mechanism cannot be provided

by the $(v/\sigma, \epsilon)$ diagram alone. For example, four among the five intrinsically most flattened COMA early-types are very close to the isotropic rotator line in Fig. 2. However, they are shaped by a combination of $\beta \gtrsim 0$ and $\gamma \lesssim 0$ (cf. Tab. 1).

3.3 Influence of a dark matter halo

The presence of dark matter around a galaxy affects the shape of the stellar orbits. Some of the models just discussed may not exist, if an additional dark matter halo reshapes the potential significantly. To check this, we have recalculated all our toy models in a potential, where a spherical, logarithmic dark halo has been added to the stellar potential. The parameters of the halo (its core radius and its asymptotic circular velocity) have been set according to the dark matter scaling relations in COMA early-types (Thomas et al. 2008). The derived anisotropies in the new potential differ in no case by more than 0.1 from the original ones (but see the discussion in App. B). Especially, the relationship between β and ϵ , that arises from the maximisation of the orbital entropy also appears in potentials with a realistic dark matter halo. This does not necessarily imply that the neglect of dark matter in models of real galaxies has no effect on the derived anisotropies, because it may enforce a redistribution of the orbits (cf. next Sec. 4).

4 REAL GALAXIES

Fig. 3 shows the connection between anisotropy and flattening in real galaxies. The intrinsic flattening of COMA galaxies is expressed in terms of

$$\epsilon = \frac{\int dR R^2 \text{SB}(R) \epsilon(R)}{\int dR R^2 \text{SB}(R)} \quad (26)$$

(Binney 2005). Here, R is the radius along the projected major-axis and $\text{SB}(R)$ and $\epsilon(R)$ are the surface-brightness

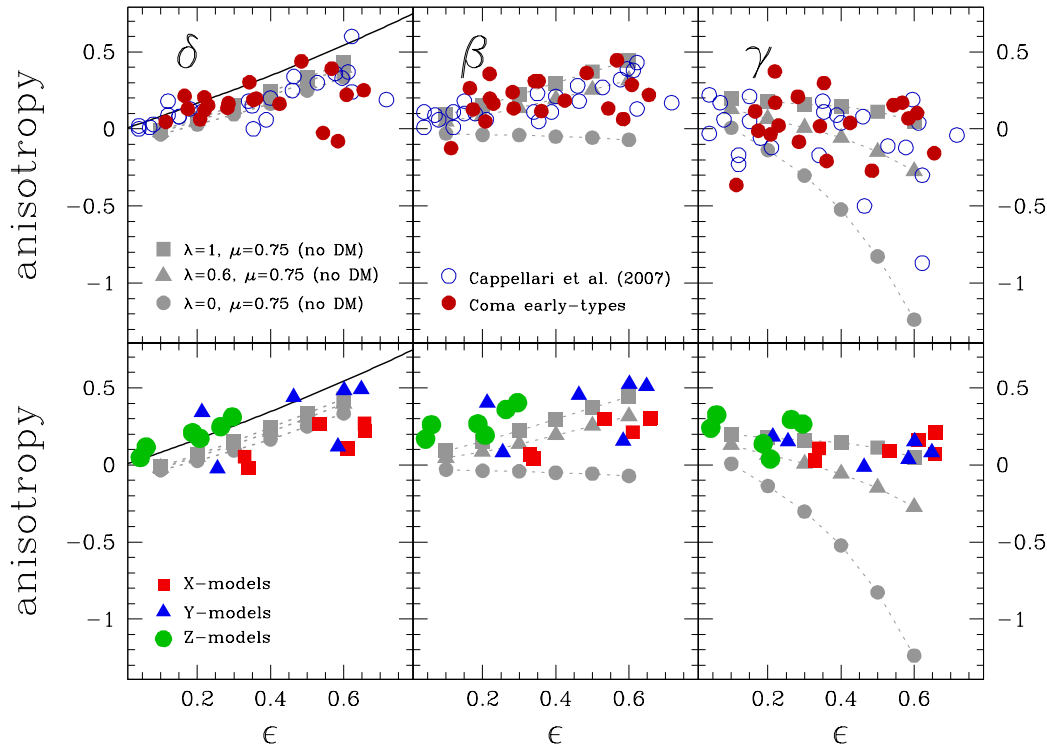


Figure 3. Top: Anisotropy parameters δ , β and γ (as labelled in the panels) versus intrinsic ellipticity ϵ for real galaxies (cf. mid panel in top row). Bottom: same for models of N -body merger remnants. Light: toy models from equation (27), connected by dotted lines. Solid lines in left panels: tensor virial theorem applied to oblate spheroids with constant flattening.

profile and ellipticity profile in the edge-on projection. For an axisymmetric system (with flattening q) $\epsilon \approx (1 - q)$.

Lines in Fig. 3 trace three different toy models

$$f_\lambda = \lambda f_S + (1 - \lambda) f_{2I} \quad (27)$$

(cf. Sec. 3; the three models are designed to rotate by using $\mu = 0.75$ in equation 24). DFs $f \approx f(E, L_z)$ are inconsistent with the global orbital structure of most galaxies (because $\beta > 0$ in observed galaxies). Most galaxies have orbital properties between those of f_S and f_{2I} (with some rotation).

Fig. 3 also includes anisotropies and flattenings of 24 early-types from Cappellari et al. (2007). These galaxies are a subsample of the 48 Es/S0s of the SAURON survey (de Zeeuw et al. 2002), which uniformly covers the plane of observed flattening ϵ_{obs} and M_B (for $M_B < -18$). The galaxies of Cappellari et al. (2007) are drawn from this survey according to various requirements, among them consistency with axial symmetry (according to 2d kinematical maps). The galaxies of Cappellari et al. (2007) (shortly SAURON in the following) are on average fainter than the COMA galaxies.

Although the samples do not match exactly, the anisotropies of COMA and SAURON galaxies are found in the same range. However, the COMA sample contains relatively more anisotropic but nearly round galaxies on the one hand and more highly flattened but isotropic galaxies

($\delta \approx 0$) on the other. As a result, the trend for δ and β to increase with ϵ which is seen in the SAURON sample is not obvious when considering the complete COMA sample (even not if the two Coma galaxies with the most uncertain anisotropies are ignored – the two central galaxies GMP2921 and GMP3329).

The relation between β and ϵ is weaker in the COMA galaxies in part due to a few round but anisotropic galaxies – for example GMP1750 and GMP5568 with $\epsilon \approx 0.2$ and $\beta \approx 0.26 - 0.36$. Both galaxies show weak minor-axis rotation (Thomas et al. 2007b) and could be slightly triaxial systems. In addition to differences among nearly round galaxies, anisotropies in COMA and SAURON galaxies also slightly differ at high ϵ . The latter is most clearly seen in δ versus ϵ : two highly flattened COMA galaxies (GMP1990 and GMP2440, $\epsilon \approx 0.6$) have $\delta \approx 0$. One of these galaxies is likely close to edge-on, because of its high observed ellipticity ($\max \epsilon_{\text{obs}} \approx 0.625$, cf. the radial profile in Thomas et al. 2007b) and its significant isophotal shape distortions. We expect the model of GMP1990 to be well constrained, because of the near edge-on inclination (minimal uncertainties in the deprojection) and its far-extending multi-slit kinematic data. For the other galaxy (GMP2440) Mehlert et al. (2000) quote only a modest observed ellipticity $\epsilon_{\text{obs}} = 0.33$ at r_{eff} and the intrinsic flattening comes mostly from the low inclination of the model. Note that this galaxy is far above the

isotropic rotator line in the right panel of Fig. 2 (GMP2440 is the only non edge-on galaxy above the isotropic rotator line). A maximum-entropy like DF is ruled out for this galaxy, because even the maximally rotating version of the f_S model would not allow for the high observed rotation rate. Thus, even if we would have underestimated the inclination of this system, Fig. 2 shows that its orbital structure must be significantly deviant from maximum-entropy models. All in all then, modelling uncertainties are unlikely to explain the outstanding anisotropies of GMP1990 and GMP2440. In fact, a comparison with Fig. 3 in Cappellari et al. (2007) reveals that the SAURON sample does not include galaxies like GMP1990 and GMP2440, because (1) for only one object the observed ellipticity is significantly larger than $\epsilon_{\text{obs}} > 0.5$ (NGC4550) and (2) even the fastest rotators in the SAURON sample are closer to the isotropic rotator line than GMP2440.

In addition to differences in the sample selection also the modelling methods differ in the details. Cappellari et al. (2007) use similar orbit-based dynamical models as we do here, but SAURON anisotropies are calculated inside a fixed aperture with a radius of $25''$. A fixed aperture encloses different fractions of the stellar mass in different galaxies, depending on system size and distance. For the COMA galaxies we give anisotropies inside r_{eff} . In some galaxies local anisotropies vary significantly with radius (Thomas et al. 2007b), such that the radius of comparison is crucial. In addition, SAURON models are based on the assumption that mass follows light. As it has been stated already in the introduction, the assumption of a constant mass-to-light ratio can result in artificially large ϕ -energies (Thomas et al. 2005, Forestell & Gebhardt 2008) or low γ , respectively. Regarding Fig. 3, SAURON galaxies do not have systematically lower γ than COMA objects. For the only two exceptions (NGC4473 and NGC4550) Cappellari et al. (2007) report evidence for counter-rotating, disk-like components that likely cause their large ϕ -energies. The small effect that the neglect of dark matter has on the anisotropies likely reflects the fact that we only consider anisotropies averaged inside $r \lesssim r_{\text{eff}}$, where the assumption that mass follows light is most closely fulfilled (e.g. Gerhard et al. 2001, Thomas et al. 2007b). For the Coma galaxies a quantitative comparison of models with and without dark matter is made in App. A.

The spatial coverage with kinematic data in the inner regions is sparse in the COMA galaxies (long-slit data) compared to the SAURON objects (2d kinematical maps). In regions of phase-space that are not well constrained by the observed kinematics, the dynamical models are mainly driven by regularisation. Thus, because the spatial coverage is lower in the COMA galaxies, their anisotropies could be biased towards the adopted regularisation scheme. Specifically, COMA galaxy models are regularised towards maximum entropy (Thomas et al. 2005). However, the middle panel in the top row of Fig. 3 does not show any bias of the COMA models towards the maximum entropy relation. In fact, SAURON galaxies are on average closer to this relation than COMA galaxies. This indicates that regularisation is not the main driver for the COMA galaxy models. Also, in App. A we give an explicit comparison of COMA galaxy models with standard and with weak regularisation. We do not find significant differences.

Both the intrinsic ellipticity and the anisotropy depend on the inclination of the models. For the COMA galaxies, we probe three different inclinations and use the one that fits best (Thomas et al. 2007b), while inclinations for SAURON galaxies are derived from two-integral Jeans models (Cappellari et al. 2006). The inclination is best constrained for highly flattened galaxies, because these have to be close to edge-on. For three of the COMA galaxies (GMP0756, GMP1176 and GMP1990) large ellipticities together with significantly discy/boxy isophotes indeed indicate close to edge-on inclinations (for example, GMP1176 exhibits $a_4 > 10$; Corsini et al. 2008). In contrast, two among the five galaxies with $\epsilon \geq 0.5$ owe their flattening in part from the relatively low inclination of the best-fit model (GMP0282, GMP2440; cf. Tab. 1). These galaxies provide the smallest and largest anisotropies, respectively, at high ϵ (cf. middle panel in the top row of Fig. 3). This suggests that the method to determine the inclination for the COMA galaxies does not result in a specific bias of the derived anisotropies.

We conclude that slight differences between the SAURON and the COMA anisotropies are mostly due to the different sample selections, while differences in the modelling methodology (including differences in the data coverage) seem to be negligible.

5 COMPARISON OF OBSERVED GALAXIES AND N -BODY MERGER REMNANTS

The lower panels of Fig. 3 display the models of N -body merger remnants (cf. Sec. 2). In terms of δ versus ϵ and β versus ϵ , these models do not differ strongly from models of real galaxies (see also Burkert et al. 2008). However, while $\gamma \geq 0$ in models of merger remnants, γ is often negative in models of real galaxies. Is this discrepancy in γ indicative for the merger remnants having a different orbital structure than real galaxies, or does it merely reflect systematics caused by the symmetry assumptions in our models?

Reconstructed and true intrinsic anisotropies³ and flattenings of the merger remnants are compared in Fig. 4. The one merger remnant closest to oblate axial symmetry (OBLATE), is reconstructed with high accuracy from the X and Y-projections (edge-on). This is plausible, because for this remnant the assumption of axial symmetry is a good approximation. Furthermore, in the edge-on case the deprojection becomes unique and the intrinsic degeneracies in the dynamics are likely smallest.

However, the general trend in the axisymmetric models is to underestimate both, the flattening and the anisotropy of the merger remnants. X and Y-projections allow a better reconstruction of shape and anisotropy than Z-projections. It has already been discussed in Thomas et al. (2007a) that the assumption of axial symmetry enforces an inclination mismatch in the Z-models: while the triaxial remnants appear flattened in the Z projection (face-on), axisymmetric

³ Note that while $\Pi_{xx} = \Pi_{yy}$ in axisymmetric systems, $\Pi_{xx} \geq \Pi_{yy}$ in the merger remnants. For the intrinsic δ of the merger remnants we use the average $(\Pi_{xx} + \Pi_{yy})/2$ instead of Π_{xx} in equation (5).

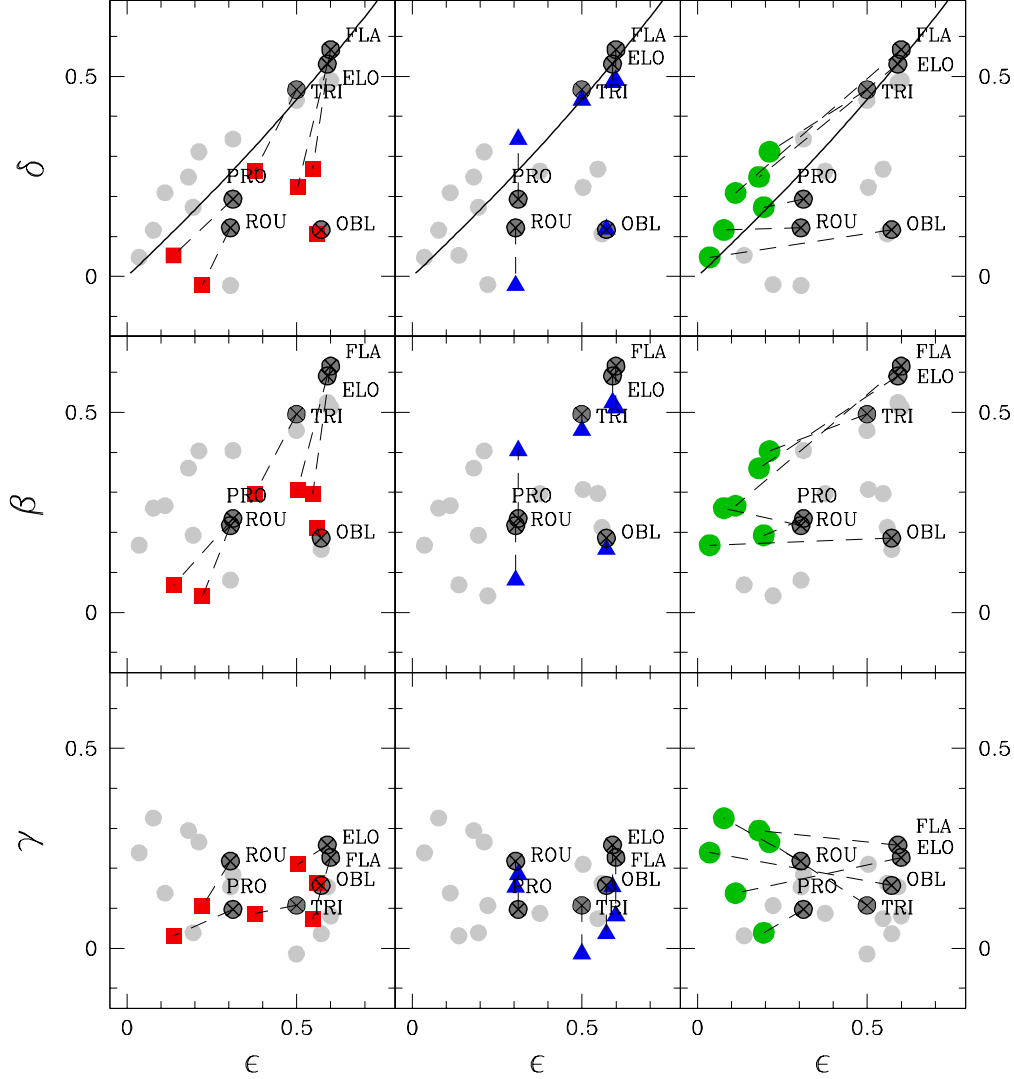


Figure 4. From top to bottom: anisotropy parameters δ , β and γ versus (intrinsic) ellipticity ϵ . Heavy symbols: intrinsic parameters of N -body merger remnants (abbreviations refer to the TRIAX, PROLATE, ROUND, FLAT, ELONG and OBLATE merger remnants discussed in Thomas et al. 2007a); light: Schwarzschild models of merger remnant projections. From left to right: models of X , Y and Z -projections are highlighted in colour. In each panel, dashed lines indicate which model belongs to which merger remnant. Solid lines in top row: $\delta(\epsilon)$ of equation (19), as in Fig. 1.

systems are necessarily round when seen face-on. Then, because the models are forced towards a wrong viewing-angle, (1) the intrinsic flattening is underestimated and (2) X , Y and Z -axes of models and remnants do no longer correspond to each other. For example, a Z -model's γ measures a different energy ratio as the remnant's γ (Thomas et al. 2007a). Had we compared the Z -models with the apparent shape of the remnant in Z -projection and with the energy ratios along axes of models and remnants that correspond to each other, then the differences would have been much smaller (for example $\Delta\epsilon < \Delta\delta \lesssim 0.1$).

Real galaxies are seen at random viewing angles. Start-

ing from our models of principal projections it is difficult to predict directly the analogous distributions of $\delta(\epsilon)$ or $\beta(\epsilon)$ for the realistic case of random projections. However, because the projections along principal axes yield extreme kinematical and photometrical properties of the merger remnants (Jesseit, Naab & Burkert 2005), it can be expected that dynamical models of projections along intermediate viewing-angles will have properties intermediate between those of the models from principal projections. We have verified this for two out of the six merger remnants (ELONG and OBLATE) by modelling additional 11 projections (at intermediate viewing-angles). Assuming that this result can

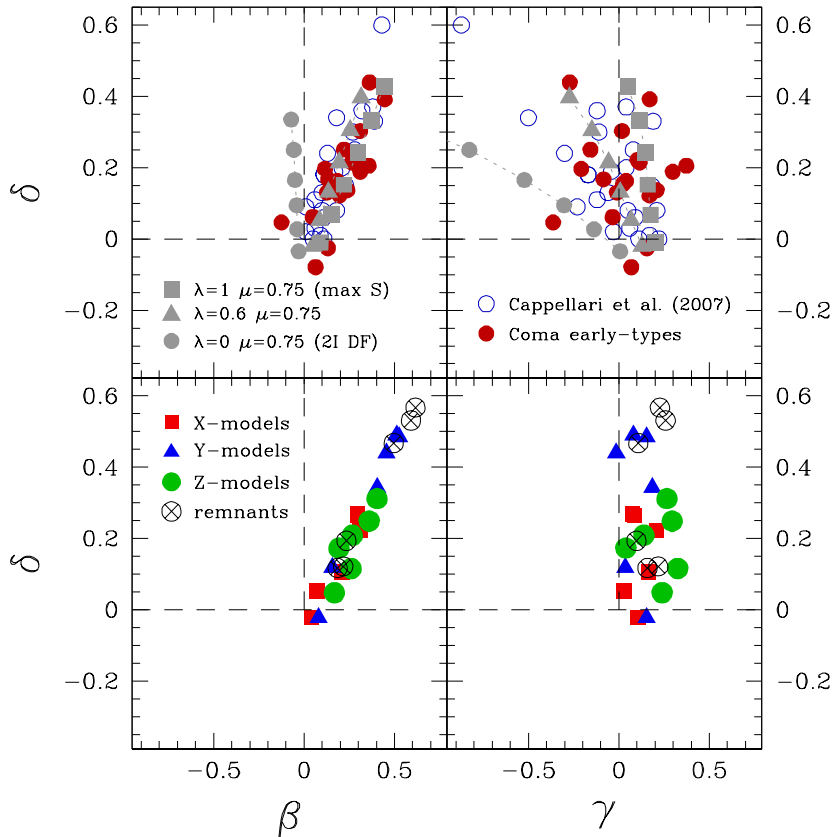


Figure 5. Correlations among the anisotropy parameters δ , β and γ . Top: models of real galaxies (squares, triangles and circles: toy models from equation 27, connected by dotted lines); bottom: models of merger remnants (squares, triangles and circles separate models of projections along different principal axes as indicated in the lower-left panel; crosses with circles: intrinsic anisotropies of the N -body remnants).

be generalised to other remnants as well, then Figs. 3 and 4 suggest the following: if real galaxies would resemble the modelled merger remnants, then one would see approximately the same relationships $\delta(\epsilon)$ and $\beta(\epsilon)$ as in the COMA and SAURON galaxies. However, it is clear from Fig. 4 that $\gamma \geq 0$, for a sample of randomly projected objects like our modelled N -body merger remnants. Thus, in this respect, models of many real galaxies differ from our comparison sample of synthetic N -body merger remnants: models of merger remnants are always radially anisotropic ($\Pi_{RR} > \Pi_{\phi\phi} \approx \Pi_{zz}$), while models of real galaxies are characterised by $\Pi_{\phi\phi} \gtrsim \Pi_{RR} > \Pi_{zz}$.

This fact is further illustrated in Fig. 5, which shows correlations among the anisotropy parameters. Even though shape and anisotropy cannot be recovered simultaneously (in some cases), the anisotropy correlations in the models of the merger remnants and in the merger remnants itself are very similar to each other. Again, the main difference between real galaxies and merger models is the offset between their γ distributions.

Besides the fact that merger remnants have on average

positive $\gamma > 0$, while real galaxies have $\gamma \approx 0$ (on average), Fig. 5 shows that the distribution of anisotropies in the merger remnants is tighter than in real galaxies. This may reflect the similarity in the initial conditions of the N -body simulations (most noteworthy the similarity in the progenitors and the fact that we only consider collisionless mergers).

6 IMPLICATIONS FOR THE FORMATION PROCESS OF EARLY-TYPE GALAXIES

The anisotropy parameters defined in Sec. 3 are only global measures of the orbital structure. A full understanding of the formation process of early-type galaxies can only be provided by spatially resolved anisotropy profiles. For example, equatorial near circular orbits obey, in the epicycle approximation, the local relation

$$\frac{\sigma_{\phi}^2}{\sigma_R^2} \approx \frac{1}{2} \left(1 + \frac{d \ln v_{\text{circ}}}{d \ln r} \right), \quad (28)$$

where v_{circ} is the circular velocity (Binney & Tremaine 1987). In a typical galaxy potential the circular velocity curve is flat ($d \ln v_{\text{circ}}/d \ln r \approx 0$) and equation (28) predicts $\sigma_\phi^2 \approx 0.5 \sigma_R^2$. Since the epicycle approximation holds for perturbed rotating disks, we do not expect the majority of early-types in our sample to be well described by equation (28). However, it might be relevant for the most flattened, rotating and discy objects in our sample. Instead, at least some of these (for example GMP1176 and GMP3958) have negative γ (i.e. $\sigma_\phi > \sigma_R$). This does not rule out a disk heating scenario for these galaxies, however, because locally we find $\sigma_\phi^2 \approx (0.5 \cdots 0.7) \sigma_R^2$ near the equatorial plane in these galaxies (around $r \approx r_{\text{eff}}$; cf. the radial anisotropy profiles in Thomas et al. 2007b).

In case of the collisionless N -body merger simulations, already the averaged anisotropy parameters reveal significant differences to the models of real galaxies. Which physical processes are responsible for this discrepancy?

The orbital structure of the models of merger remnants is largely driven by a population of central box orbits in the N -body systems (Thomas et al. 2007a). They cause the centres of the merger remnants to become triaxial/prolate and are, for example, largely responsible for the wrong viewing angle of the Z-models. Dissipation during a merger can have a significant effect on the shape and the projected properties of the final remnant (Barnes & Hernquist 1996; Cox et al. 2006; Robertson et al. 2006; Naab, Jesseit & Burkert 2006; Jesseit et al. 2007). Already 10 percent of gas are sufficient to suppress central box orbits and to produce an approximately axisymmetric remnant in binary mergers (Naab, Jesseit & Burkert 2006) (but this result is based on simulations without star formation).

Multiple, simultaneous minor mergers likewise produce remnants less triaxial than collisionless binary merger remnants (Weil & Hernquist 1996), but the corresponding kinematics have not yet been studied in detail. Successive minor merging does not necessarily lead to different final remnants, at least if the cumulative merged mass becomes similar to the most massive progenitor (Bournaud, Jog & Combes 2007). Again, detailed predictions for the orbital make-up and the shapes of the line-of-sight velocity distributions have not yet been worked out.

Note that the central dark matter densities in COMA ellipticals are larger than in present-day spirals (Thomas et al. 2008). Even if ellipticals have formed by some variant of merging, present-day spiral galaxies are unlikely the progenitors for the bulk of giant ellipticals (see also Naab & Ostriker 2007). Burkert et al. (2008) pointed out that N -body systems, which have assembled hierarchically in their cosmological simulations (Naab et al. 2007), or by binary mergers with star-formation and black-hole feedback are consistent with the trend between δ and ϵ in observed galaxies.

7 SUMMARY

We have discussed the relationship between anisotropy and flattening in toy models, in models of real galaxies, in merger remnants and in models of merger remnants. Models of observed galaxies generally exhibit $\beta > 0$ and $\gamma \approx 0$. We do

not find strong correlations of the anisotropy parameters δ , β and γ with intrinsic ellipticity ϵ .

In toy models with maximum entropy for a given density distribution we find β to increase with ϵ , while $\gamma \lesssim 0$. Observed galaxies appear close to these maximum-entropy relations, but exhibit a large degree of individuality. Rotation appears in anisotropic ($\beta > 0$) as well as isotropic systems ($\beta \approx 0$), suggesting that the flattening of the galaxies largely arises from a suppression of stars with large energies perpendicular to the equatorial plane. This is similar to the classical notion of flattening by anisotropy and rules out DFs $f \approx f(E, L_z)$ for most early-type galaxies.

The global similarity between models of observed galaxies and our maximum-entropy toy models suggests that early-type galaxies are largely relaxed stellar systems. However, there are differences in the details that probably contain valuable information about the assembly mechanism of the galaxies and will be addressed in a future paper.

Numerical simulations indicate that both strongly radially anisotropic ($\gamma \rightarrow 1$) and strongly tangentially anisotropic systems ($\gamma \ll 0$) can become unstable (e.g. Merritt & Stiavelli 1990; Sellwood & Merritt 1994; Nipoti et al. 2002). Maximum entropy models have intermediate anisotropies and are likely stable. Thus, the anisotropies of observed galaxies may not only be understood as being the most likely ones (in the sense of yielding the maximum entropy at a given flattening) but could also reflect stability constraints. So far we lack detailed studies exploring the stability of axisymmetric systems with dark matter halos and various intrinsic anisotropies. Since our (three integral) toy models can be easily transformed to N -body systems (cf. Thomas et al. 2007a) they provide a suitable tool to setup both artificially anisotropic as well as realistic and observationally motivated initial conditions.

In models of real galaxies the unordered kinetic energy in the azimuthal direction, $\Pi_{\phi\phi}$, can exceed the radial energy Π_{RR} by up to 40 percent. This separates real galaxy models from similar models of collisionless N -body binary disk mergers, which are instead characterised by radial anisotropy ($\Pi_{RR} > \Pi_{\phi\phi} \approx \Pi_{zz}$). Because we have applied the same modelling machinery to both, the real galaxies as well as the synthetic N -body merger remnants, our findings indicate a true difference between their intrinsic properties. Especially, we have shown that if real galaxies would resemble our merger remnants, then corresponding dynamical models of real data would be radially anisotropic, irrespective of the systematics introduced by the assumption of axial symmetry.

The radial anisotropy of the merger remnants is related to a population of central box orbits. Because dissipation during a merger can efficiently suppress box orbits, our results suggest that dissipation played an important role during the formation of intermediate mass to massive early-type galaxies.

In this paper we focussed on the comparison of real galaxies with collisionless binary disk merger simulations. A similar analysis, but for gaseous mergers with star formation and/or for galaxies formed in cosmological simulations could give more insight into the actual formation paths of elliptical galaxies.

ACKNOWLEDGEMENTS

This work was supported by DFG Sonderforschungsbereich 375 ‘‘Astro-Teilchenphysik’’ and DFG priority program 1177. EMC receives support from grant CPDA068415/06 by Padua University.

REFERENCES

- Barnes J. E., 1992, *ApJ*, 393, 484
 Barnes J. E., Hernquist L., 1996, *ApJ*, 471, 115
 Bender R., Möllenhoff C., 1987, *A&A*, 177, 71
 Binney J., 1978, *MNRAS*, 183, 501
 Binney J., Tremaine S., 1987, *Galactic Dynamics* (princeton: Princeton University Press)
 Binney J., 2005, *MNRAS*, 363, 937
 Bournaud F., Jog C. G., Combes F., 2007, *A&A*, 476, 1179
 Burkert A., Naab T., 2005, *MNRAS*, 363, 597
 Burkert A., Naab T., Johansson P. H., Jesseit R., 2008, *ApJ*, 685, 897
 Cappellari M. et al., 2006, *MNRAS*, 366, 112
 Cappellari M. et al., 2007, *MNRAS*, 379, 418
 Carollo C. M., de Zeeuw P. T., van der Marel R. P., Danziger I. J., Qian E. E., 1995, *ApJL*, 441, 25
 Contopoulos G., 1963, *AJ*, 68, 1
 Corsini E. M., Wegner G., Saglia R. P., Thomas J., Bender R., Thomas D., 2008, *ApJS*, 175, 462
 Cox T. J., Jonsson P., Primack J. R., Somerville R. S., 2006, *MNRAS*, 373, 1013
 Dehnen W., 1993, *MNRAS*, 265, 250
 Dehnen W., Gerhard O. E., 1993, *MNRAS*, 261, 311
 Dehnen W., Gerhard O. E., 1994, *MNRAS*, 268, 1019
 Dubinski J., 1998, *ApJ*, 502, 141
 Forestell A., Gebhardt K., 2008, *astro-ph0803.3626*
 Gebhardt K. et al., 2000, *AJ*, 119, 1157
 Gebhardt K. et al., 2003, *ApJ*, 583, 92
 Gerhard O. E., Kronawitter A., Saglia R. P., Bender R., 2001, *AJ*, 121, 1936
 Godwin J. G., Metcalfe N., Peach J. V., 1983, *MNRAS*, 202, 113
 Hernquist L., 1990, *ApJ*, 356, 359
 Hernquist L., 1992, *ApJ*, 409, 548
 Hernquist L., 1993, *ApJ*, 400, 460
 Jesseit R., Naab T., Burkert A., 2005, *MNRAS*, 360, 1185
 Jesseit R., Naab T., Peletier R. F., Burkert A., 2007, *MNRAS*, 376, 997
 Jørgensen I., Franx M., 1994, *ApJ*, 433, 553
 Kormendy J., 1982, in Martinet L., Major M., eds, *Morphology and Dynamics of Galaxies*. Geneva Observatory, Geneva, p. 113
 Krajnović D., Cappellari M., Emsellem E., McDermid R. M., de Zeeuw P. T., 2005, *MNRAS*, 357, 1113
 Lynden-Bell D., 1962, *MNRAS*, 124, 1
 Magorrian J., Ballantyne D., 2001, *MNRAS*, 322, 702
 Magorrian J., 2006, *MNRAS*, 373, 425
 Mehlert D., Saglia R. P., Bender R., Wegner G., 2000, *A&AS*, 141, 449
 Merritt D., Stiavelli M., 1990, *ApJ*, 358, 399
 Naab T., Burkert A., 2003, *ApJ*, 597, 893
 Naab T., Jesseit R., Burkert A., 2006, *MNRAS*, 372, 839
 Naab T., Ostriker J. P., 2007, *astro-arXiv:astro-ph/0702535*
 Naab T., Johansson P. H., Ostriker J. P., Efstathiou G., 2007, *ApJ*, 658, 710
 Nipoti C., Londrillo P., Ciotti L., 2002, *MNRAS*, 332, 901
 Richstone D. O., Tremaine S., 1988, *ApJ*, 327, 82
 Roberts P. H., 1962, *ApJ*, 136, 1108
 Robertson B., Cox T. J., Hernquist L., Franx M., Hopkins P. F., Martini P., Springel V., 2006, *ApJ*, 641, 21
 Rybicki G., 1987, in de Zeeuw T., ed., *Proc. IAU Symp.* 127, *Structure and Dynamics of Elliptical Galaxies*, Reidel, Dordrecht, p. 397
 Schwarzschild M., 1979, *ApJ*, 232, 236
 Sellwood J. A., Merritt D., 1994, *ApJ*, 425, 530
 Thomas J., Saglia R. P., Bender R., Thomas D., Gebhardt K., Magorrian J., Richstone D., 2004, *MNRAS*, 353, 391
 Thomas J., Saglia R. P., Bender R., Thomas D., Gebhardt K., Magorrian J., Corsini E. M., Wegner G., 2005, *MNRAS*, 360, 1355
 Thomas J., Jesseit R., Naab T., Saglia R. P., Burkert A., Bender R., 2007b, *MNRAS*, 381, 672
 Thomas J., Saglia R. P., Bender R., Thomas D., Gebhardt K., Magorrian J., Corsini E. M., Wegner G., 2007a, *MNRAS*, 382, 657
 Thomas J., Saglia R. P., Bender R., Thomas D., Gebhardt K., Magorrian J., Corsini E. M., Wegner G., 2008, *ApJ* in press
 Valluri M., Merritt D., Emsellem E., 2004, *ApJ*, 602, 66
 van Albada T. S., 1982, *MNRAS*, 201, 939
 Wegner G., Corsini E. M., Saglia R. P., Bender R., Merkl D., Thomas D., Thomas J., Mehlert D., 2002, *A&A*, 395, 753
 Weil M., Hernquist L., 1996, *ApJ*, 457, 51
 de Zeeuw P. T. et al., 2002, *MNRAS*, 329, 513

APPENDIX A: THE INFLUENCE OF REGULARISATION AND DARK MATTER ON RECONSTRUCTED GALAXY ANISOTROPIES

The Coma galaxy models discussed in this paper are derived using our standard regularisation parameter $\alpha = 0.02$ (cf. equation 9). The strength of the standard regularisation has been calibrated by means of Monte-Carlo simulations of isotropic rotators (Thomas et al. 2005). To check how much the choice of α affects our results, we (1) determined the best-fit dynamical model at $\alpha = 1$ and (2) recalculated the anisotropies of all galaxies from these weakly regularised models (at $\alpha = 1$, the minimum χ^2 is usually reached). In the top row of Fig. A1 we show both models with standard and with weak regularisation for comparison. As can be seen, lowering the regularisation has almost no effect on the derived anisotropies. Especially, there are still at least four galaxies with significantly negative $\gamma < 0$.

In the bottom row of Fig. A1 we make a similar comparison for models with and without dark matter: squares indicate the anisotropies of our best-fit models with a constant mass-to-light ratio (no dark matter halo). As expected, when assuming that mass-follows-light, γ become smaller (the amount of ϕ -energy is increased to compensate for the missing dark mass). From the bottom-right panel one would expect that the average γ becomes negative when the radial increase of the mass-to-light ratio (caused by a dark halo) is neglected. This is not the case in the SAURON

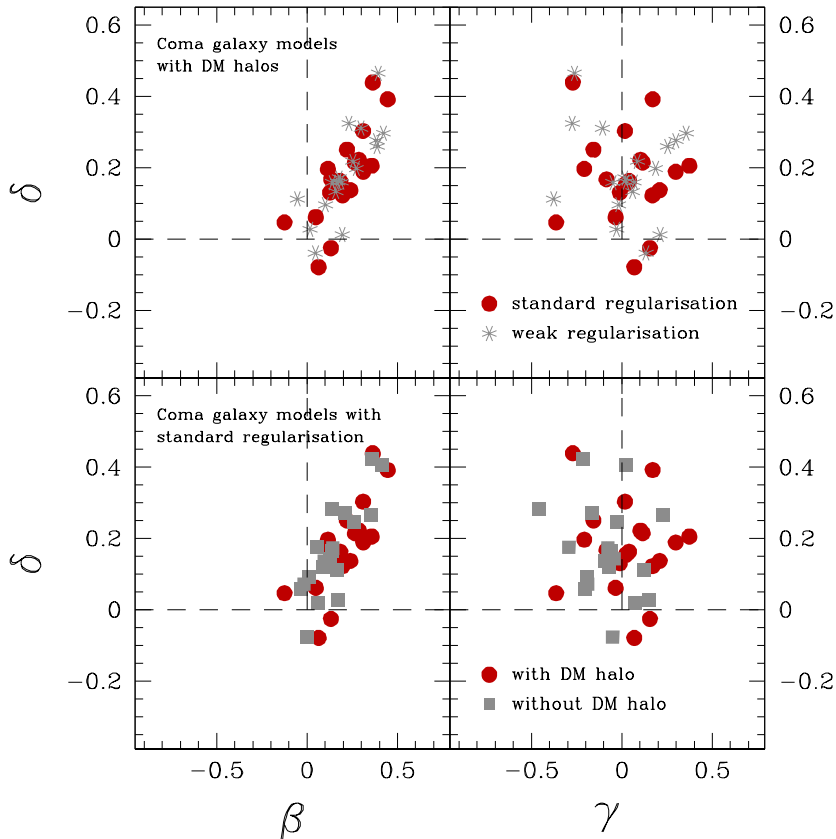


Figure A1. As Fig. 5, but in the top row Coma galaxy models are plotted with standard regularisation (filled circles; $\alpha = 0.02$ in equation 9) and with weak regularisation (stars; $\alpha = 1$). The bottom row shows Coma galaxy models with (filled circles) and without (squares) dark matter halos (in both cases the standard regularisation was applied).

sample, however, although Cappellari et al. (2007) assumed that the mass-to-light ratio is constant with radius in their models. That neglecting dark matter has a stronger effect in Coma galaxies is likely related to the fact that our kinematical data reach out into the region where dark matter becomes noticeable ($\gtrsim r_{\text{eff}}$), which is probably not the case in many SAURON galaxies (where the data extend only out to $\lesssim r_{\text{eff}}$).

APPENDIX B: THE RADIALY RESOLVED ANISOTROPY STRUCTURE OF MAXIMUM-ENTROPY TOY MODELS

The maximum-entropy toy models f_S discussed in Sec. 3.1 resemble the classical flattening by anisotropy, except that they are only approximately isotropic in R and Φ . To investigate where this anisotropy comes from, we have constructed maximum-entropy toy models in potentials that include a dark matter halo. The halo density distribution is assumed to follow

$$\rho_{\text{DM}} \propto m^{-\eta}(m+1)^{\eta-4} \quad (\text{B1})$$

(Dehnen 1993). To mimick realistic halos (cf. Thomas et al. 2007b) we choose a flat central density core ($\eta = 0.05$) and we set the flattening q of the halo equal to the flattening of the luminous component of the toy model (cf. equation 13). We investigated three mass models: (1) no halo, (2) a mass model that has a roughly constant circular velocity curve and (3) a mass model with a rising v_{circ} in the outer parts of the model. The corresponding circular velocity curves for $q = 0.7$ are shown in the bottom panels of Fig. B1.

The upper panels of Fig. B1 display the radial profiles of the local anisotropies

$$\beta_{\text{eq}}(r) \equiv 1 - \frac{\sigma_z(r)^2}{\sigma_R(r)^2} \quad (\text{B2})$$

and

$$\gamma_{\text{eq}}(r) \equiv 1 - \frac{\sigma_\phi(r)^2}{\sigma_R(r)^2} \quad (\text{B3})$$

along the equatorial plane (averaged within $|\vartheta| \leq \pm 11.5^\circ$, where ϑ is the latitude). As one can see, the anisotropy in the meridional plane (β_{eq}) does not depend on the shape of the gravitational potential. Thus, the relation between β

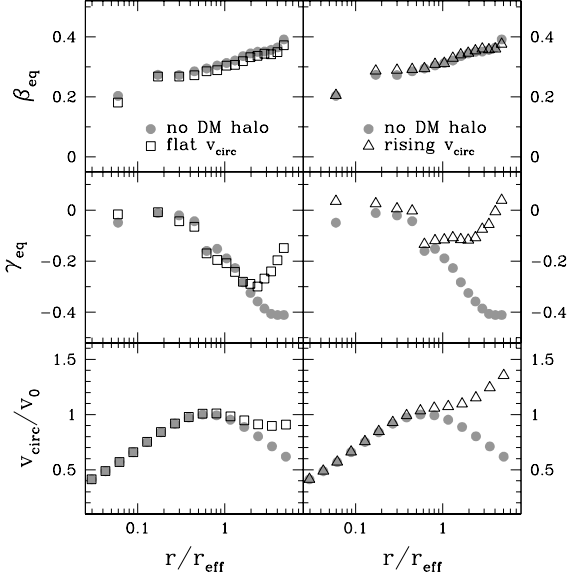


Figure B1. Radial anisotropy profiles β_{eq} (top) and γ_{eq} (middle) for maximum-entropy models (f_S ; flattening $q = 0.7$) with dark matter halos. Left-hand side/squares: halo tuned to result in an approximately flat circular velocity curve; right-hand side/triangles: halo leading to an increasing circular velocity in the outer parts of the model. For comparison, the case without halo is shown on both sides (circles). Circular velocity curves of the models (scaled to the maximum circular velocity v_0 without halo) are shown in the bottom panels.

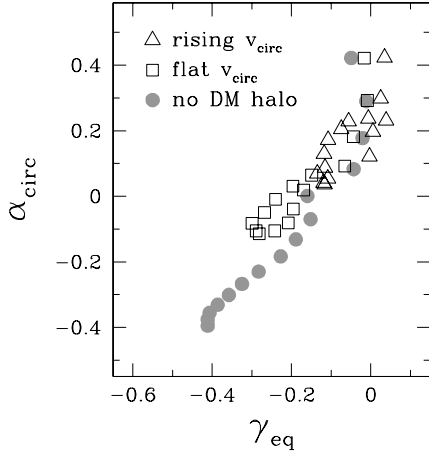


Figure B2. Local anisotropy γ_{eq} (along the equatorial plane) versus logarithmic slope $\alpha_{\text{circ}} \equiv d \ln v_{\text{circ}} / d \ln r$ of the circular velocity curve. Symbols and colours as in Fig. B1.

and ϵ is largely independent from the gravitational potential and closely related to the entropy maximisation.

However, beyond r_{eff} , where dark matter starts to influence the shape of the circular velocity curve, γ_{eq} is different in the three different potentials. Fig. B2 shows that the local value of γ_{eq} – along the equatorial plane – is directly connected to the logarithmic slope α_{vcirc} of the circular velocity curve. In general then, because γ from equation (7) is the spatial average of γ_{eq} (and the local anisotropies along other position angles in the meridional plane), its exact value is not set uniquely by the entropy maximisation but also depends on the shape of the circular velocity curve. In practice, however, deviations with respect to the model without halo become noticeable only beyond r_{eff} , such that even the spatially averaged γ of the toy models does not depend strongly on whether a halo is included or not.

Note that the relation revealed by Fig. B2 is different from the epicycle relation (28). This is expected, because the azimuthal velocity dispersion σ_ϕ in the toy models largely results from the fact that they do not rotate. Instead, the dispersion predicted by the epicycle approximation arises from perturbations on circular orbits in a rotating disk.